Comparison of Endwall Loss Reduction Techniques in a High-Lift Turbine Passage

Christopher R. Marks[1]
U.S. Air Force Research Lab,
Wright-Patterson AFB,
OH 45433
e-mail: christopher.marks.6@us.af.mil

Nathan Fletcher
Innovative Scientific Solutions Inc.,
Dayton, OH 45459

Rolf Sondergaard
U.S. Air Force Research Lab,
Wright-Patterson AFB,
OH 45433

The development of techniques that reduce the losses in the endwall region is an important area of research as it supports an increase in the turbine design space through the use of higher lift blade designs while maintaining high efficiency. Several active and passive shape contouring methods that reduce losses generated by the secondary flow have been developed and investigated on a high-lift front-loaded low-pressure turbine research profile in a low-speed linear cascade configuration. This paper summarizes and compares alterations to the three-dimensional secondary flow field by the application of three different techniques: blade profile contouring, optimized endwall shape contouring, and localized low mass coefficient jets. Each method was applied to identical research blade profiles and compared in the same linear cascade wind tunnel resulting in a unique perspective into the loss reduction mechanisms associated with each technique. The design strategy will be discussed along with a detailed description of changes to the secondary flow field using in- and out-of-passage total pressure loss measurements and high-speed stereoscopic particle image velocimetry. The key findings include the loss reduction mechanisms associated with each approach and the manipulation of key endwall flow structures such as the passage vortex and a strong suction surface corner separation. [DOI: 10.1115/1.4050599]

Keywords: turbine aerodynamic design, fluid dynamics and heat transfer phenomena in compressor and turbine components of gas turbine engines

1 Introduction

Progress in numerical design techniques and computational speed have supported research efforts toward the expansion of the low-pressure turbine (LPT) aerodynamic design space. The LPT accounts for a considerable portion of the overall engine size and weight. Researchers have noted the potential for improved blade designs to positively impact the weight [1], cost, and part count of the engine. Praisner et al. [2] showed that the historical trend is moving toward reducing the number of airfoils in the LP turbine to decrease both the engine weight and life-cycle cost. Two key design parameters that drive weight and part count are the work output per stage and the blade loading coefficient. These two parameters can be manipulated during design to impact the footprint and the performance of the LP turbine section by increasing the loading of each blade [3].

As blade loading is increased in the LPT, aerodynamic challenges must be overcome to maintain the high efficiency of modern designs. These challenges include low Reynolds number conditions at engine cruise, and complex three-dimensional vortical flows in the passage hub and tip regions. The former can lead to laminar boundary layer separation resulting in an increase in profile losses and a decrease in loading. In the endwall region, high-lift blade designs augment secondary losses due to an increase in endwall surface area with stronger three-dimensional flows. Each of these phenomena pose a challenge to numerical design tools. The design and subsequent verification in a high-speed rotating turbine facility of a highly loaded LPT is described in Schmitz et al. [3]. The design process included the use of three-dimensional unsteady Reynolds-averaged Navier–Stokes (RANS). Detailed experimental measurements in the rotating turbine facility confirmed good overall agreement with the design predictions; however, modeling challenges remained in the endwall and secondary flow regions [3].

While the basic mean secondary flow model has been known for years, see for example the review paper of Langston [4], there is on-going computational and experimental research by several groups working toward better physical understanding and modeling of high-lift LPT aerodynamics. Various loss reduction strategies for the secondary flow region have been developed including passive techniques such as endwall surface shaping or contouring [5–7], profile contouring near the blade/endwall junction [8–12], and endwall fences [13,14]. These approaches are typically optimized for a single flow condition. Active flow control (AFC) techniques have also been proposed, which can be employed in an on-demand fashion and optimized in real-time to perform efficiently over a range of flow conditions. However, AFC is more complex to implement, consists of additional hardware, and requires energy input. Studies that have attempted AFC in turbines often involve fluid injection and/or removal to strategically disrupt certain flow features. Bloxham and Bons used suction holes on the endwall to either remove the low momentum fluid from the passage vortex (PV) or to alter the cross-passage trajectory of the vortex in a high-lift LPT passage [15]. Both strategies resulted in loss reductions. Benton et al. [16] used pitched/skewed steady jets along the suction surface which forced the PV away from the SS to achieve significant loss reduction. Large momentum coefficients were used with steady jet actuation; however, lower mass flowrates were also found to be effective when the jets were pulsed [17]. It was also thought that at one particular pulsing frequency, natural instabilities in the flow field were taken advantage of allowing for more efficient loss reduction.

Low mass ratio (MR) localized wall-normal jet actuation in the vicinity of the pressure side leg of the horseshoe vortex was investigated using high-fidelity numerical simulation by Gross et al. [18]. The simulations showed that the secondary flow could be manipulated through such a technique; however, the early simulations resulted in a modest improvement in total pressure loss. Related

experiments in a low-speed linear cascade were developed with a similar localized jet arrangement, described in Refs. [19–21], with each study finding that the jet arrangement resulted in a loss reduction and manipulation of the three-dimensional secondary flow.

The present work focuses on secondary loss reduction strategies for high-lift LPT airfoils. Detailed measurements of endwall profile contouring, endwall shape contouring, and localized low mass ratio endwall jets are brought together to describe their influence on aerodynamic loss generation through a low-speed linear cascade of front-loaded high-lift airfoils. Portions of data collected and reported separately in Refs. [21–25] are combined with new data and analysis to provide insight into the flow physics associated with each of the three different secondary flow loss techniques.

2 Loss Reduction Techniques

Sections 2.1–2.4 describe the secondary flow field and loss generation through the high-lift front-loaded research profile used in the present study, followed by a summary of the three different loss reduction techniques detailed in this paper.

2.1 Endwall Flow Description. A series of high-lift airfoil profiles were designed at the U.S. Air Force Research Laboratory (AFRL) to study the low Reynolds number aerodynamics which challenge numerical design codes. Each profile maintains the same design inlet and exit angles as the Pratt and Whitney Pack B profile flow geometry. The incompressible Zweifel coefficient (Zw) spans 1.34–1.59 across the series of airfoils. In addition to varying the loading coefficient, the peak loading location was also varied resulting in high-lift profiles with front, mid, and aft loading.

The front-loaded L2F profile ($Zw = 1.59$) described in Ref. [26] is used in the present study. The blade has a 38% greater loading level than the Pack B airfoil. The design process resulted in a high-lift airfoil with good mid-span Reynolds lapse characteristics.

The L2F has been the subject of numerous detailed cascade studies into the secondary flow physics in the passage of a front-loaded high-lift airfoil. An Implicit Large Eddy Simulation (ILES) of the passage flow was developed and compared with the experiments in Gross et al. [27]. The numerical model showed excellent agreement with low-speed cascade measurements including three-dimensional secondary flow structures and total pressure loss generation. A diagram of the dominant time-averaged secondary flow structures is shown in Fig. 1(a). The incoming boundary layer separates as it encounters the passage pressure gradient. A horseshoe vortex structure is formed at the leading-edge junction with the endwall. One leg of the vortex moves toward the suction surface, and the other toward the pressure side. These two vortices are often referred to as the suction side and pressure side legs of the horseshoe vortex, abbreviated here as SSHV and PSHV. The PSHV extends across the passage toward the suction surface of the adjacent blade forming a vortex line. In the case of the front-loaded L2F airfoil, both the ILES and numerous experiments have shown the SSHV decreases in strength rapidly as it moves along the L2F suction surface side of the passage.

The incoming boundary layer separates along the primary separation line (not shown) followed by a separated shear layer that rolls up into the PSHV vortex core line which extends from near the pressure side blade leading edge across the passage. Both simulations and experiments (e.g., Refs. [28,29]) have shown that the vortex intermittently loses coherence, fluctuates in strength, and its position undulates in the pitchwise direction. The vortex core line is strengthened by the secondary flow across the passage. The three-dimensional structure is referred to as the PV as it extends across the passage and interacts with a strong corner separation near the suction surface trailing edge. An additional vortex structure is generated along the suction surface corner separation with the same sense of rotation as the PSHV and PV, see cross section in Fig. 1(a). This rotational structure is referred to as the suction
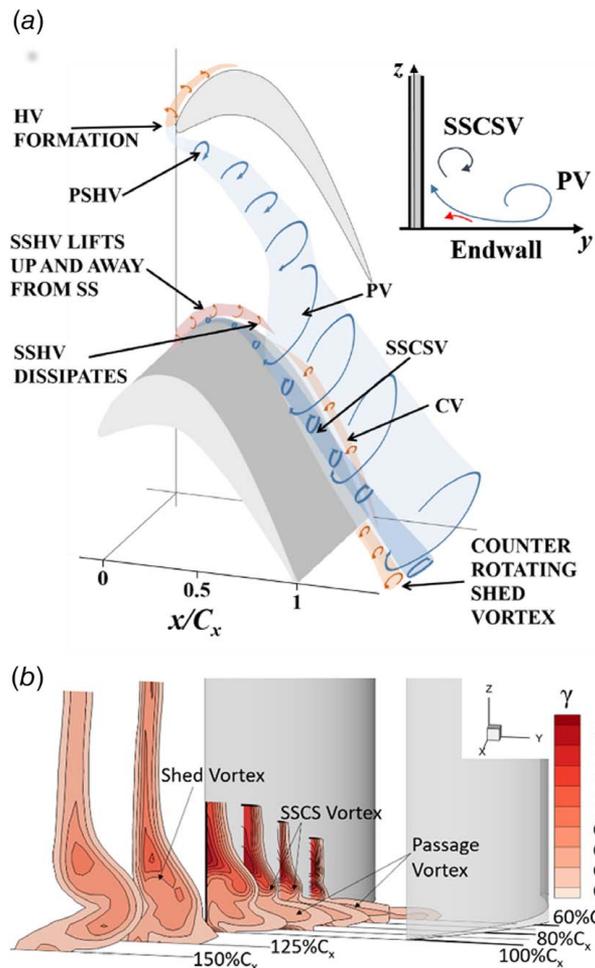

Fig. 1 L2F secondary flow: (a) diagram describing the dominant endwall vortical structures and (b) experimental measurements of total pressure loss development (data from Ref. [22])

side corner separation vortex (SSCSV). At the trailing edge, an additional vortex structure extends downstream with opposite sense of rotation labeled as the counter rotating shed vortex. Additional detailed discussion of the L2F mean secondary flow can be found in Refs. [22,27].

Total pressure loss development through the passage is shown in Fig. 1(b) using measurements from Ref. [22]. The mean secondary flow structures can be related to the regions of high-loss, with the loss breakdown process initiated primarily through shear. While there is a region of elevated loss in the vicinity of the PV, the largest region of loss generation occurs in the area of the SSCSV where there is strong interaction with both the PV and mean flow along the suction surface located above the SSCSV.

2.2 Profile Contouring. Three different profile contours have been developed for the L2F profile and tested in a low-speed linear cascade wind tunnel. Each of the three shapes are shown in Fig. 2, from two different viewing perspectives. The diagrams in the top row were generated from the computational design, and the photographs in the bottom row show the test articles. Each profile is a variation of a low stagger angle, high-lift profile shape called the L2F-LS described in Lyall et al. [10]. The low stagger profile produced less endwall losses; however, it generated greater profile losses than the L2F shape. The L2F-LS profile was blended into the L2F shape at the endwall to produce the first "fillet" like shape labeled as the EF [10]. The L2F-EF configuration produced reduced secondary losses through the passage. Two additional
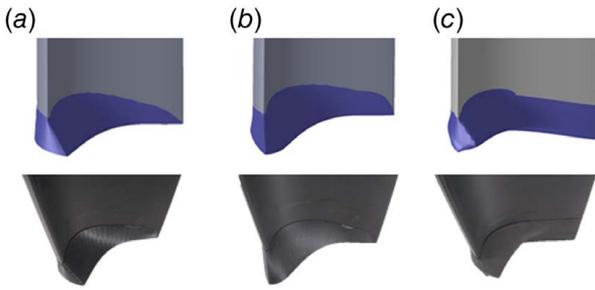
Fig. 2 Endwall profile contour shapes, two different viewing angles are shown for clarity: (a) L2F-EF, (b) L2F-EF2, and (c) L2F-EB

variations of the profile contouring were developed, the EF2 and EB shapes, which were first described in Refs. [12,30]. The EF2 shape maintained the low stagger angle of the L2F-LS profile with a variation of the leading-edge angle, which has been rotated so that it aligns with design inlet flow angle at the stagnation point. A third shape was generated by blending the L2F-LS with L2F a distance away from the endwall at the incoming boundary layer thickness rather than the junction of the blade with the endwall. This produced a "bulb" like shape that was labeled as the EB, which resembles a blended fence shape on the pressure surface that wraps around the leading edge and extends along the suction surface.

2.3 Endwall Contouring. Two different endwall contour shapes have been designed for the L2F profile, as shown in Fig. 3. The first shape could be called typical of those found in the open literature and is referred to as EWC1. The design and experimental validation of the EWC1 was described in Ref. [23]. The second contour was described by Dickel et al. [24] using a genetic algorithm (GA) with downstream total pressure loss as the cost function. The GA resulted in a highly contoured shape with a hill near the leading-edge pressure surface, long narrow ridge through the passage near the suction surface, and a deep valley along the suction surface. The numerical design process and experimental validation is described in Ref. [24].

2.4 Localized Endwall Jets. Numerical simulations in Ref. [18] investigated the use of localized fluidic forcing in the endwall region to reduce secondary flow losses. Steady and pulsed disturbances with small mass ratios were introduced in the vicinity of the leading edge adjacent to the PSHV to perturb the endwall flow. The simulations found that the localized fluid injection resulted in a small reduction in total pressure loss and weakened the coherence of the passage vortex. In a similar manner, experiments were developed in a low-speed linear cascade to further investigate the arrangement including the effect of jet parameters on pressure loss. The localized low mass ratio endwall jet

arrangement is shown in Fig. 4. A circular array of small mass ratio wall-normal jets were positioned near the PV liftoff line, and experimental measurements are described in Refs. [19,20]. Babcock et al. [21] investigated the changes in total pressure loss through L2F passages under the influence of the jets. In-passage total pressure loss distributions from Ref. [21] are combined with new results from an expanded measurement campaign to better assess the relationship between passage total pressure loss reductions and localized jet parameters (e.g., mass ratio, frequency, and jet duty cycle (DC)). New in-passage velocimetry measurements which focus on the time-averaged secondary flow response with high and low duty cycle jets are also presented in this paper. Further analysis of the dynamic response of the secondary flow to jet actuation using high-speed stereo particle image velocimetry (SPIV) can be found in Ref. [25].

3 Experimental Setup

All experimental measurements were acquired in the AFRL Low-Speed Wind Tunnel Facility's linear cascade. The test section was configured with seven linear L2F blades. A splitter plate was installed for secondary flow studies and is shown in Fig. 5. The plate extended upstream and downstream from the cascade to generate a clean incoming boundary layer. The outline of the splitter plate is similar to the cascade configurations described in Ref. [31]. The splitter plate had an elliptic leading-edge profile, and its length could be varied to produce various boundary layer states.

The baseline flow conditions and blade parameters are listed in Table 1. It should be noted that the passage had a large aspect ratio (AR) 4.17 and relatively thin incoming boundary layer thickness relative to span (2.2%H) compared with many other endwall studies in the literature.

All measurements were obtained with an incoming Reynolds number of 1.0×10^5 based on incoming flow velocity and blade axial chord. The incoming flow velocity was measured using a Pitot-static probe mounted $1.5C_x$ upstream from the cascade leading edge. The dynamic pressure was measured by a 0–0.4 in H_2O Druck pressure transducer. Total pressures loss measurements were acquired by measuring the difference between a downstream total pressure probe and the upstream total pressure. Total pressure loss coefficient γ was calculated by normalizing the total pressure loss measurement by incoming dynamic pressure

$$\gamma = \frac{p_{t,in} - p_{t,out}}{\frac{1}{2}\rho U_{in}^2} \tag{1}$$

Total pressure loss measurements were made using a custom in-line Kiel probe described in Ref. [32]. In-passage measurements were obtained by traversing a single in-line Kiel probe. Total pressure loss coefficient measurements downstream of the passage were obtained by traversing a rake of five total pressure probes across
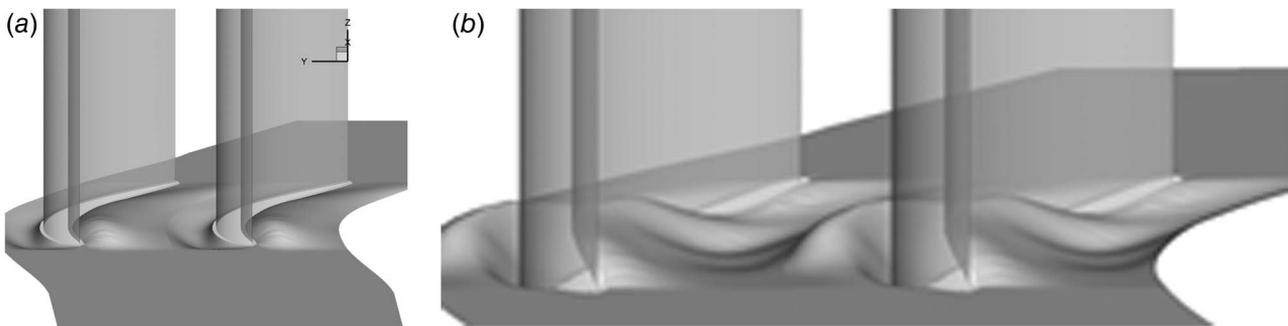

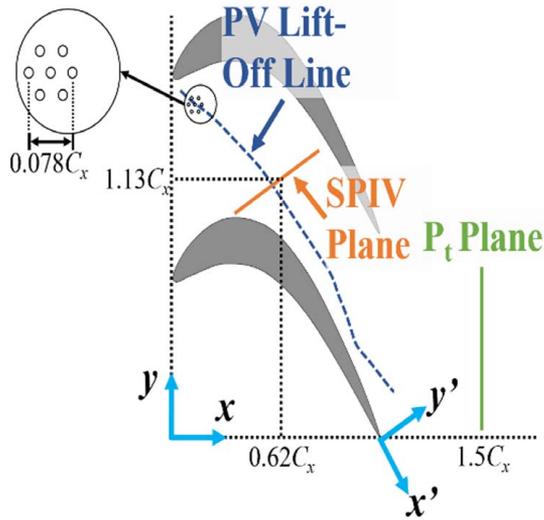**Fig. 3 L2F endwall contour shapes [23,24]: (a) EWC1 and (b) EWC2**
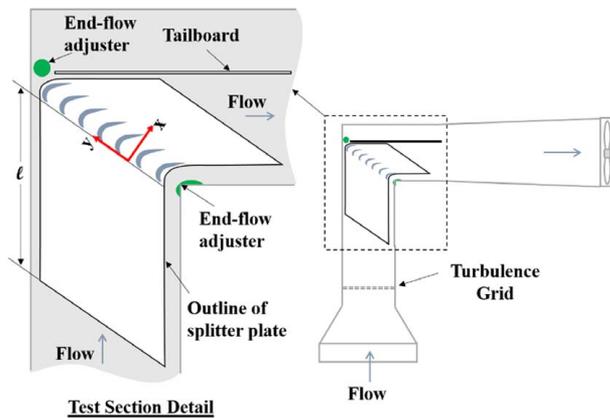
Fig. 4   Localized endwall jet configuration

Fig. 5   Linear cascade wind tunnel layout—top view

one-pitch and from the endwall up to 40% span. Integral values of total pressure loss coefficient (γ_{PS}) reported in Sec. 4.2 are area-averages of the passage measured $1.5C_x$ downstream from the cascade leading edge. Differences in integrated passage total pressure loss coefficient of the modified endwall flow compared with the baseline planar endwall geometry ($\Delta\gamma_{PS}$) are used to compare the benefit of each technique. The total pressure loss data in this paper are from multiple experimental measurement campaigns, and the delta loss coefficients are calculated relative to the individual baseline loss value obtained for each measurement campaign to provide the most self-consistent assessment of loss reduction provided by each technique. Significant effort was spent obtaining reliable and repeatable integrated total pressure loss data. The

Table 1   Linear cascade dimensions and inlet conditions

Axial chord, C_x	15.24 cm
Pitch/axial chord, S/C_x	1.221
Cascade span/axial chord, AR, H/C_x	4.17
Inlet design flow angle (from axial), α_{in}	35 deg
Exit design flow angle, α_{ex}	−60 deg
Inlet Reynolds number	1.0×10^5
Design Zweifel coefficient (Zw)	1.59
Freestream turbulence intensity	3%
Boundary layer thickness	2.2%H

uncertainty of total pressure loss coefficient (γ) measurements in exit plane is estimated at ± 0.0025. Numerous measurements of the area-averaged total pressure loss at the baseline flow conditions resulted in an uncertainty of less than $\pm 0.25\%$ based on repeatability.

The velocity field through the passage in the endwall region was measured using high-speed SPIV. Two Phantom VEO 640L 4 MP cameras in combination with a Photonics DM30 Dual Head 527 nm Nd:YLF 30 mJ laser were used to acquire image pairs. A LaVision Programmable Timing Unit (PTU) and DAVIS 8 software were used to control timing, calibrate, acquire, and calculate the velocity vector fields from each raw image pair. Additional image processing of the vector fields was accomplished using in-house processing codes. Measurements were acquired at ~2.5 kHz. Final spatial resolution was typically 1.1 vectors/mm (167.8 vectors/C_x). The location of the laser sheet and SPIV measurement plane are shown in Fig. 4. The plane was aligned perpendicular to the exit flow direction and placed across the passage to capture the characteristics of the passage vortex.

Q-criterion, Q, is used to visualize and estimate the rotational strength of vortices and calculated using Eq. (2) for 2D velocity information [33]

$$Q = -\frac{1}{2}\left[\left(\frac{\partial u}{\partial x}\right)^2 + \left(\frac{\partial v}{\partial y}\right)^2\right] - \frac{\partial u}{\partial y}\frac{\partial v}{\partial x} \qquad (2)$$

Values are calculated using the velocity components with respect to the secondary coordinate system (in-plane) and normalized using C_x and U_{in}. Time-averaged velocity vectors and Q-criterion calculated from the SPIV are included in the present paper. A minimum of 12,500 instantaneous image pairs were acquired and averaged for each case. Further detailed analysis using the high-speed SPIV data set to describe the response of the passage secondary flow to the localized endwall jets was included in Ref. [25].

Surface oil flow visualization was used to quickly assess changes in the secondary flow topology due to the various loss reduction strategies. The technique consisted of spraying a thin layer of a mineral oil and fluorescent dye mixture across the endwall surface. The tunnel flow was turned on and the surface stresses redistributed the oil mixture highlighting the near wall flow structures such as the path of the PV and the corner separation. In some cases, isopropanol was added to the mixture which resulted in a streaked pattern showing the skin friction direction, making it easier to identify separation points. An ISSI Inc. high-power LED lamp (460 nm) was used to illuminate the oil/dye mixture. Two LaVision 5 MP sCMOS cameras were used to acquire images that when stitched together showed the entire passage from $0.3C_x$ upstream of the leading edge to the trailing edge. The camera lenses were fitted with 532 nm bandpass filters to image the oil/dye mixture resulting in a high contrast image.

For the localized endwall jets, measurements were collected at different blowing conditions by varying pulsing frequency, duty cycle (percentage of time the valves are open), and for comparison: steady and baseline (no blowing) runs. Frequency is expressed as a reduced frequency

$$F^+ = \frac{f \cdot SSL}{U_{PS}} \qquad (3)$$

made dimensionless by the mean convective time of flow through the passage. The magnitude of blowing, blowing ratio (BR), is determined by the ratio of the peak jet velocity to cascade inlet velocity (Eq. (4)). This was found from a jet characterization study using a TSI 1211-20 hot-film connected to a TSI IFA-300 anemometer system with the sensor mounted immediately above the center of the center jet hole outside of the tunnel

$$BR = \frac{\overline{U_{jet,max}}}{\overline{U_{in}}} \qquad (4)$$

In actual application in a gas turbine engine, the pressurized air feeding this pneumatic system would come at a cost since it would have to be supplied from the compressor. Energy is expended to compress the air in the compressor. The air would be bled off and bypass the combustor, therefore, not performing work. In order to comparatively assess this cost among different blowing settings, the mass ratio was defined

$$MR = \frac{1}{2} \overline{\left(\frac{U_{jet}}{U_{in}}\right)} \frac{\pi N D_{jet}^2}{H \cdot S \cdot \cos(\alpha_{in})} \times 100\% \qquad (5)$$

where the ratio of the jet mass injection to that of the mass flux through half of the passage (assuming the AFC method is implemented on both endwalls). This definition is consistent with similar studies, see for example Ref. [16]. It was assumed that the jet velocity (from the hot-film results) is uniform over the area of the jet and the same for each jet hole. Likewise, the momentum coefficient, C_μ, is similarly defined

$$C_\mu = \frac{1}{2} \overline{\left(\frac{U_{jet}}{U_{in}}\right)^2} \frac{\pi N D_{jet}^2}{H \cdot S \cdot \cos(\alpha_{in})} \times 100\% \qquad (6)$$

4 Results

4.1 Secondary Flow Structures. The baseline L2F secondary flow was described in Sec. 2.1. New oil flow visualization along the endwall surface is shown in Fig. 6 with the time-averaged velocity field in the SPIV measurement plane shown in the inset. The flood of Q-criterion from the SPIV has been overlaid on the oil flow image to highlight the region of rotational flow associated with the PV. A circular portion of the oil flow image where the localized endwall jet holes were located has been blanked out. The location of the PV and strong corner separation can be identified by demarcation lines between regions where the surface stresses change direction and magnitude. Along these boundaries the oil and dye accumulates providing a visual indication of near wall flow features. Two such signatures can be easily identified in the images and have
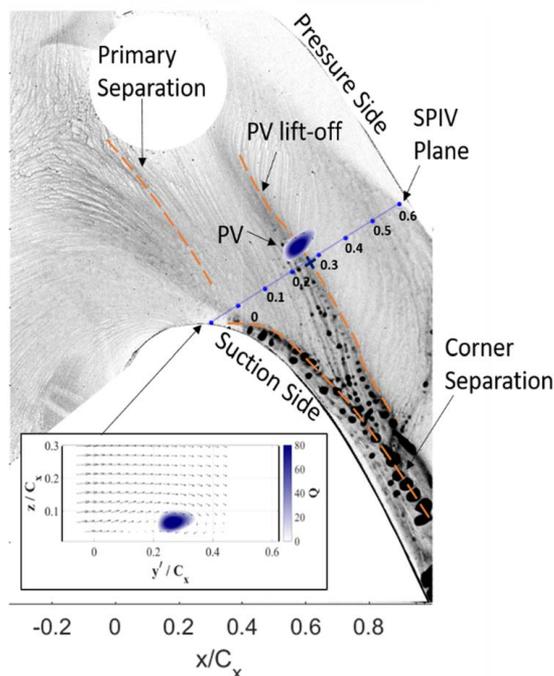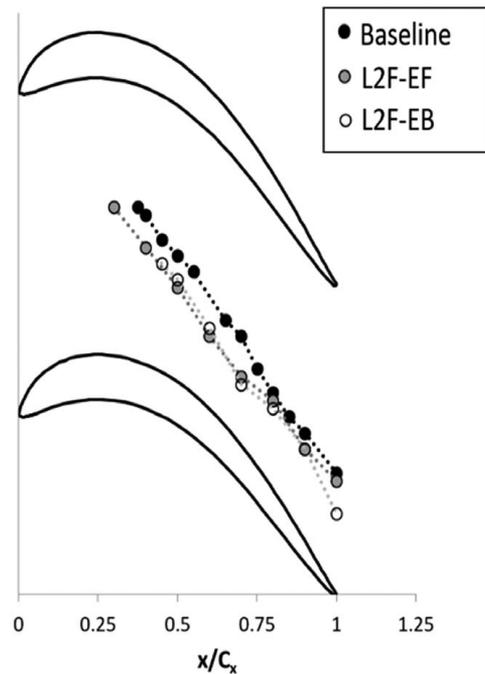

Fig. 7 Vortex positional shift due to various profile contouring designs

been labeled as "PV liftoff line" and "corner separation line." A more thorough analysis of the L2F endwall topology based on ILES was included in Ref. [27]. The analysis showed two saddle points associated with a primary and secondary separation line. The PV liftoff line is the secondary separation line corresponding to the location of the PV. The overlap in the time-averaged position of the vortex based on velocity measurements compared with the PV liftoff line shows excellent agreement between the two data sets. The existence of the corner separation line is indicative of a strong interaction between the flow between the primary and secondary separation lines and the suction surface as described by Sieverding [34].

With agreement between the PV position and liftoff line established, the location of the PV liftoff line was extracted from the endwall oil flow visualization to visualize the change in the position of the PV when different profile contours (Fig. 7), and endwall jets configurations (Fig. 8), were used. The application of either profile moves the position of the PV forward in the passage compared with the baseline, with the EF producing the greatest shift in position. The location of the primary separation was also observed to shift upstream and the saddle point toward the pressure side when the profile contouring was applied. This equates to a reduction in the distance between the primary and secondary separation lines and the amount of low momentum flow migrating toward the suction surface corner separation region. Numerous planes of Q contours throughout the passage of the cascade for both the baseline flow case and EF profile were compared in Refs. [11,22]. Both studies found a decrease in inlet boundary layer separation and a weaker PV that had shifted forward in the passage when the EF profile was used, in agreement with the present oil flow visualization.

The application of the localized endwall jets produced a similar, but larger upstream shift in the PV location. Steady jet actuation resulted in the greatest reduction in distance between the primary and secondary separation lines compared with the profile contouring.

Time-averaged Q-criterion floods calculated from the vector field measurements for the L2F-EF profile contouring and endwall jet cases are compared in Fig. 9. The background of each image
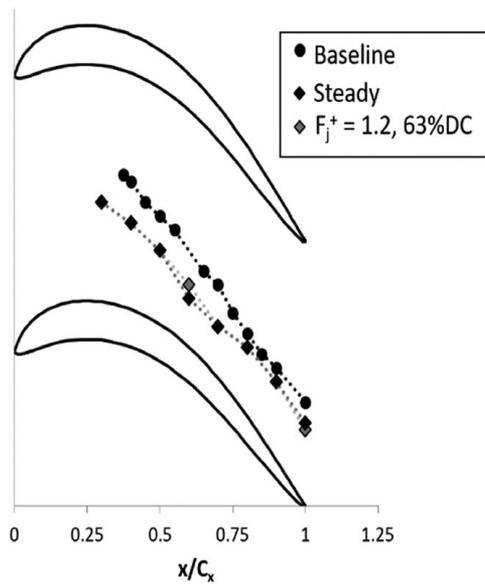

Fig. 6 L2F with planar endwall surface oil flow visualization overlaid with time-averaged Q-criterion flood from SPIV measurements

Fig. 8 Vortex positional shift due to steady and pulsed localized jets

shows the time-averaged velocity vectors for the baseline case with Q-criterion flood. The $Q = 20$ contour for each case was superimposed on the baseline field to provide a comparison of the mean vortex position and strength. The PV decreased in strength when the profile contouring, pulsed or steady jets were used (Fig. 9(a)). The largest decrease in vortex rotational strength occurred with profile contouring. The endwall jets produced a larger positional shift toward the blade suction surface consistent with the oil flow visualization. Two vortices were present in the mean flow with steady jet actuation. A weaker PV is generated that has shifted toward the suction surface, while a second structure is present toward the pressure surface (right side of image in Fig. 9). This second structure is believed to be the result of the jet oriented in cross-flow which is well known to produce streamwise vortices [25]. A weak signature of the pressure side vortex was also visible in the steady jet oil flow visualization.

The PV position and strength under various jet pulsing are compared in Fig. 9(b) to the baseline unactuated case. The vortex
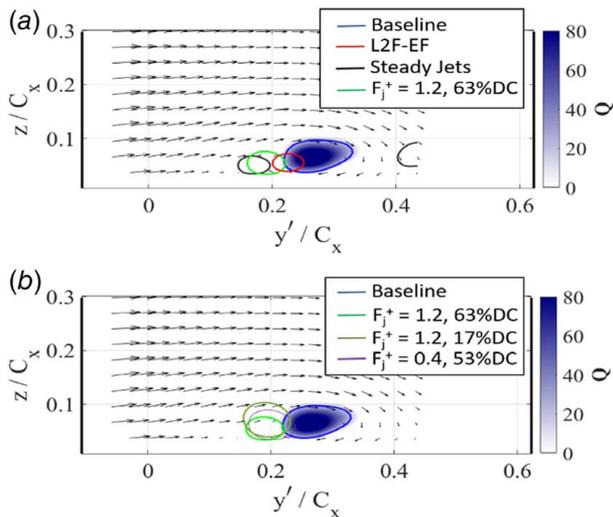

Fig. 9 Comparison of PV positional shift: (a) baseline flow compared with profile contouring and localized endwall jets and (b) baseline flow compared with various jet pulsing frequencies

position also shifted and its strength was reduced when the jets were pulsed. Comparing pulsing at $F_j^+ = 1.2$ with a high and low DC shows that the vortex position changes are similar for both case; however, the higher DC and mass ratio is required to produce a large reduction in the strength. At the reduced frequency of $F_j^+ = 0.4$, the vortex positions shifted without a major reduction in strength.

4.2 Loss Development. The influence of both the profile contouring and the endwall jets on the separation lines and passage vortex strength is evident from the oil flow visualization and in-passage SPIV measurements. Total pressure loss coefficient was measured in two-dimensional planes through the passage to show loss generation. The loss generation with profile contouring is shown compared with the baseline case in Fig. 10. The L2F-EF loss contours were compared with the L2F baseline in Ref. [22]. Sequential planes of SPIV along with an ILES of the endwall flow were used to describe loss generation in relation to the vortical structures. Findings included that the L2F-EF profile resulted in a reduction in the losses associated with the PV and a compression of the secondary flow losses toward the endwall. The profile contour reduced the strength of the loss associated with the PV; however, the loss corresponding with the SSCSV remains the same. This proved to be true for the other profile contours as well. Further investigation of the profile contour effectiveness at various Reynolds numbers and incoming boundary layer states were included in Ref. [12]. The performance benefit of each of the profiles was found to be dependent on the Reynolds number. The L2F-EF and L2F-EF2 produced the largest overall reduction in loss across the conditions tested; however, at the lowest Reynolds numbers investigated ($Re = 3.0 \times 10^4$ and 5.0×10^4), the L2F-EB design provided the best performance. The benefit of the L2F-EB was found to be optimal when the blending of fence-like feature into the blade occurred at a distance approximately equal to the boundary layer thickness away from the endwall.
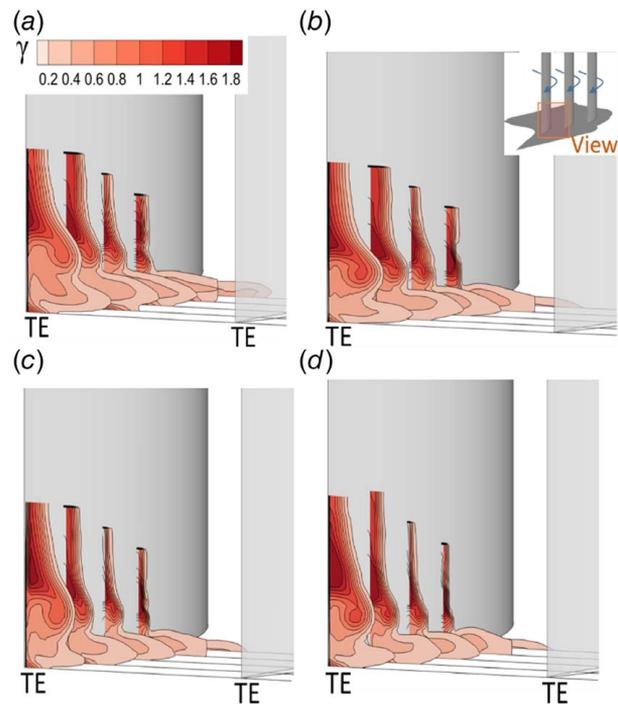

Fig. 10 Experimental measurements of secondary loss development through a passage with endwall profile contouring (data from Ref. [22]): (a) L2F, (b) L2F-EF, (c) L2F-EF2, and (d) L2F-EB
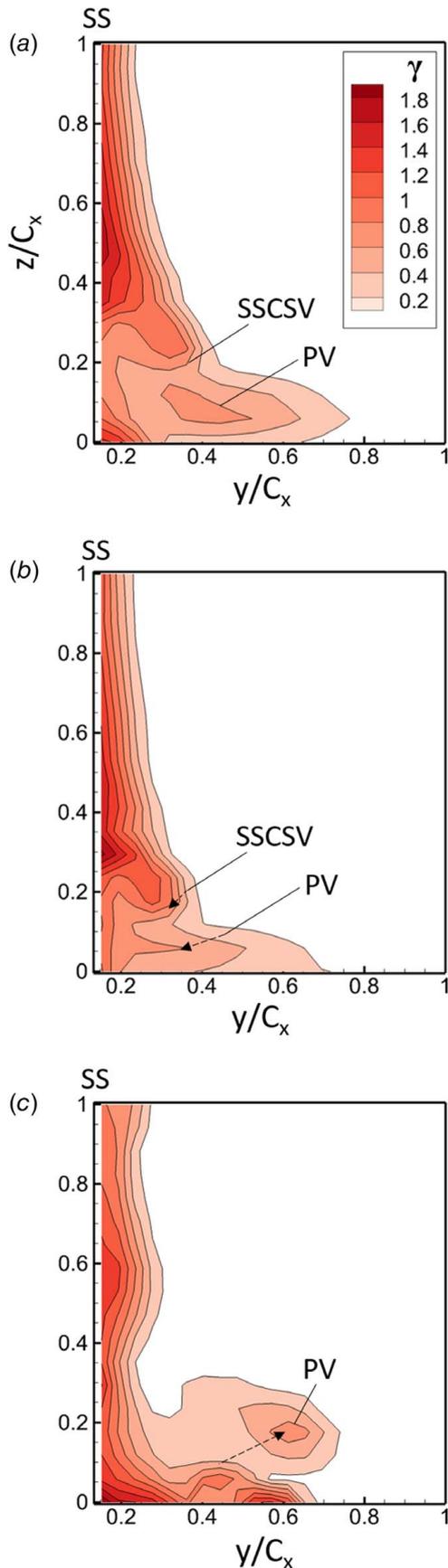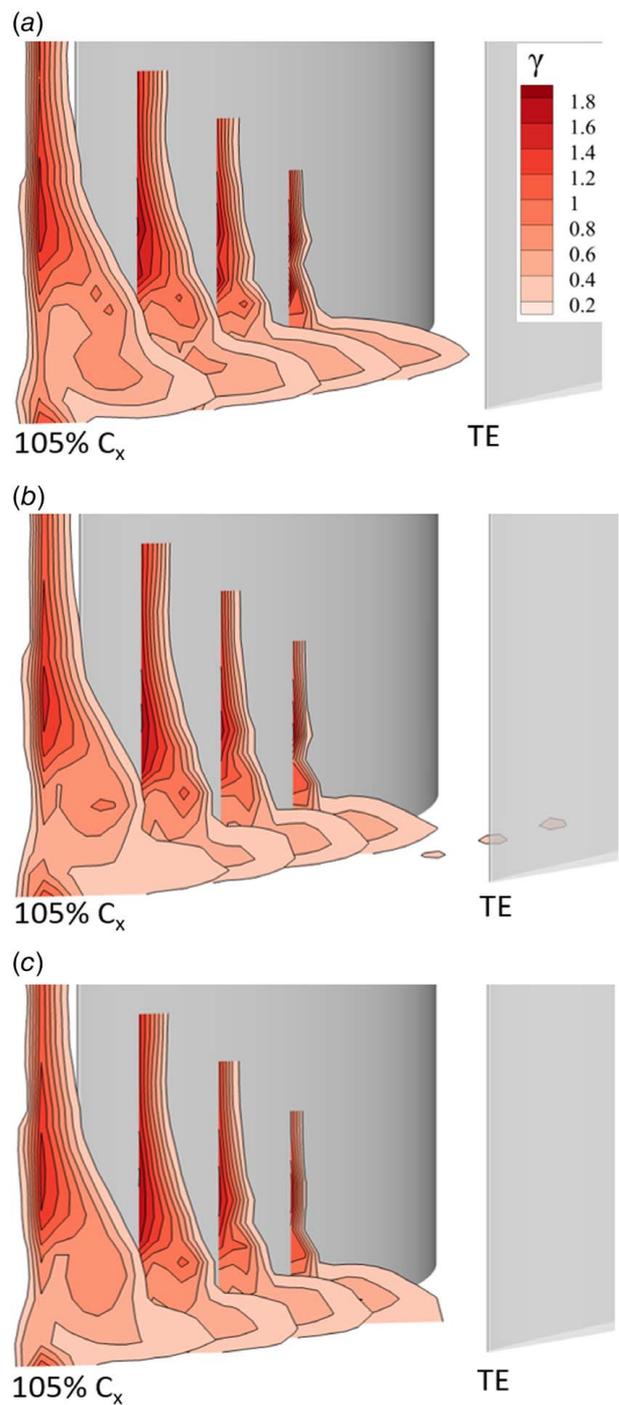
Fig. 12 Secondary loss development with application of localized steady and pulsed jets (data from Ref. [21]): (a) jets off, (b) steady jets MR = 0.08%, and (c) pulsed $F_j^+ = 1.2$, MR = 0.06%, $C_\mu = 0.23\%$, $BR = 4.3$

Fig. 11 Comparison of secondary total pressure loss distribution in the passage (95%C_x plane) with a planar and contoured endwall (data from Refs. [23,24]): (a) planar, (b) EWC1, and (c) EWC2

Total pressure loss distributions at the passage exit with the two endwall contours compared with the planar endwall are shown in Fig. 11. Both contours resulted in significant changes to the secondary loss distribution. The EWC1 produced a reduction in the extent of the upper loss region associated with the SSCSV; however, the loss core was more concentrated, suggesting a stronger roll-up and shear. The lower loss region associated with the PV corner separation was broader in the pitch direction but reduced in strength. The GA optimized EWC2 resulted in the most radical changes to the loss distribution of all cases considered. The upper

hook-like loss region associated with SSCSV was no longer present. The losses in the corner region are reduced significantly compared with the planar endwall configuration. The loss associated with the PV has been shifted away from the endwall due to the shape contouring. This minimizes the interaction of the PV with the suction surface flow, reducing the loss in the corner region.

Total pressure loss development for the localized endwall jets is shown in Fig. 12 with measurements from Ref. [21]. The steady jet case has a more noticeable effect on the loss development near the endwall than the profile contouring cases. The loss associated with the PV region of the flow has reduced significantly and shifted upstream. The loss generated along the interface of the PV and SSCSV has reduced significantly at the exit of the passage. An additional region of loss is noticeable along the pressure side of the passage for the steady jet case. This region is believed to be due to the vortical structure noted in the SPIV of Fig. 9, an artifact of the jet and interruption of the PSHV roll-up.

Pulsed jets were also able to reduce loss to the same degree as the steady jets, but using lower mass ratios. Figure 12(c) shows the loss development when the jets were pulsed just above a reduced frequency of unity with a duty cycle of 50%. The MR is 25% lower for the pulsed case but still produces a noticeable reduction in losses associated with PV.

The jets were pulsed across a range of frequencies with fixed ~50% duty cycle and MR to determine whether there was a frequency dependence, or more specifically whether the endwall dynamics would respond to certain forcing frequencies. The total pressure loss reduction compared with the baseline unactuated case is shown in Fig. 13(a). Error bars on the percent change in total pressure loss are provided for select frequencies based on

student t-distribution of multiple measurements at those frequencies.

The greatest loss reduction occurred when the jets were pulsed near a reduced frequency of unity. The cyclic response of the passage vortex at various pulsing conditions is discussed in detail in Refs. [20,25]. The strength of the passage vortex responded in a cyclic manner to pulsing. The jets had a strong effect on the strength and pitchwise location; however, the PV dynamics did not become fully dependent on the pulsing time period. This means phase averaging based on the pulsing signal will reveal an underlying cyclic behavior but may not capture the full strength and movement of the vortex. The high-speed SPIV did not reveal a sustained loss of coherence at any of the frequencies investigated.

The large decrease in loss when pulsed near unity is believe to be due to the combination of jet array characteristics, flow response, and duty cycle (~50%). Detailed measurements of the jet array are included in Ref. [25] which show a sustained effect on the flow approaching that of a steady jet, when the jet array was pulsed at $F_j^+ = 1.2$ and 50%DC.

Finally, the DC was varied to as low as 14% at pulsing frequencies of 1.2 and 0.4. This produced a variation in MR and more cyclic jet actuation at $F_j^+ = 1.2$. All pulsed jet and steady jet conditions are plotted together versus MR in Fig. 13(b). The points are colored by actuation frequency (steady jets cases are star symbols). A strong relationship between loss reduction and MR is observed. Pulsing the jets near unity provided roughly 30% greater reduction in total pressure loss compared with the steady jets operating near the same MR.

Finally, Fig. 14 and Table 2 are included as summaries of the effect of each technique on the passage total pressure loss. Figure 14 shows the downstream pitchwise integrated total pressure loss coefficient along the span. The loss profile of the L2F baseline flat endwall is comprised of two loss cores. The upper loss core is linked to the corner separation and extent of the SSCSV. The lower loss core can be associated primarily with the passage vortex. In the case of the endwall profile contours, there was some reduction in the magnitude of the upper loss core and compression of the secondary loss toward the endwall; however, the lower loss core associated with the PV was reduced considerably.

The localized endwall jets produced less compression of the upper loss core toward the endwall, primarily producing a large reduction and compression of the lower loss core toward the endwall. This supports the conclusion that the endwall jets primarily influence the secondary separation line, passage vortex strength, and interaction with the corner separation.
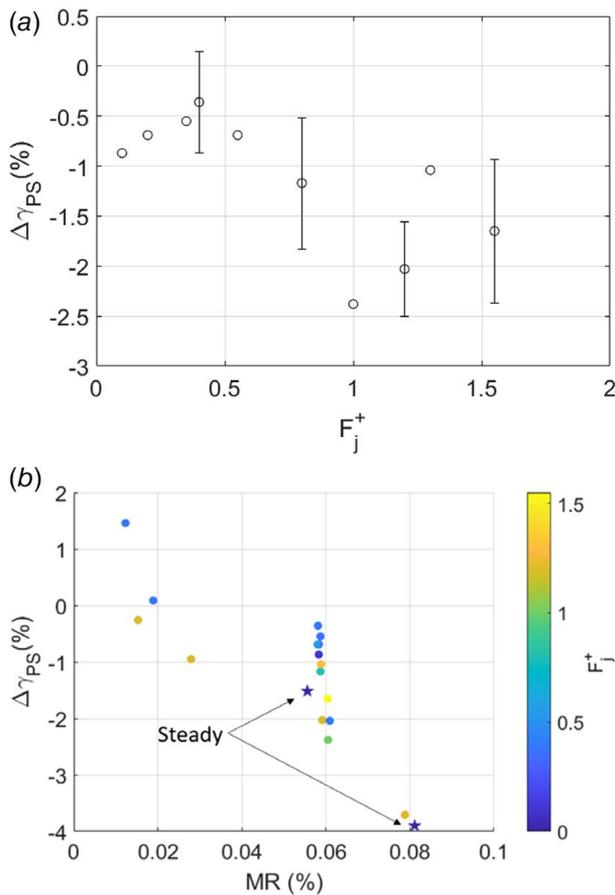

Fig. 13 Endwall jet total pressure loss reduction as a function of (a) pulsing frequency, with a constant DC and MR and (b) MR shaded by pulsing frequency
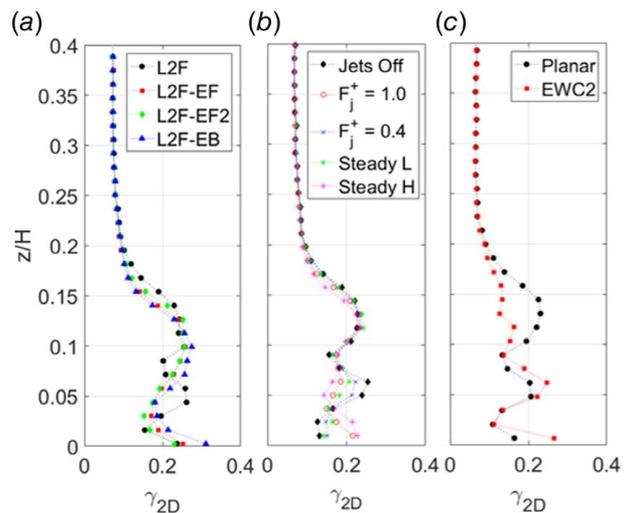

Fig. 14 Pitchwise integrated total pressure loss distribution along the span, downstream 1.5C_x plane: (a) profile contours [12], (b) localized endwall jets, and (c) optimized endwall contour [24]

Table 2 Summary of passage total pressure loss reduction

Case	$\Delta\gamma_{PS}$ (%)
L2F-EF [12]	−5.2
L2F-EF2 [12]	−4.7
L2F-EB [12]	−3.2
EWC1 [23]	−7.8
EWC2 [24]	−8.6
Steady jets (MR 0.06%)	−1.5
Steady jets (MR 0.08%)	−3.9
Pulsed $F_j^+ = 1$ (MR 0.06%)	−2.4

In contrast to the other techniques, the optimized endwall contour EWC2 reduced the losses in the upper loss core significantly with a minor reduction in the lower loss core [1]. Of the three methods described, the GA endwall contouring was the only method that primarily acted to reduce the losses in the strong corner separation. From a design standpoint, the most effective secondary loss reduction strategies will need to focus on both loss mechanisms.

The largest passage loss reduction was obtained with the endwall contouring. The GA optimized contour resulted in slightly higher loss reduction compared with EWC1. The profile contouring technique resulted in the second highest reductions in loss followed by the endwall jets. It should be noted that both the profile contouring and endwall shape contouring were developed using a numerical design process. In contrast, the localized endwall jet configuration was initially simulated using high-fidelity design tools; however, the positioning and orientation were not optimized.

5 Conclusions

Three different endwall loss reduction strategies were implemented in a low-speed linear cascade of front-loaded high-lift LPT research profiles—referred to as the L2F profile. Measurements were made with the same passage aspect ratio, Reynolds number, and incoming boundary layer characteristics. The first technique, profile contouring, consisted of blending in a low stagger angle profile into the original L2F profile at or near the junction with the endwall. Three different blending approaches were discussed in this paper. The second method involved contouring the endwall shape to reduce losses. The final method used an array of low mass ratio localized endwall jets placed near the leading edge. Both pulsed and steady actuation was discussed.

The comparison of endwall flow manipulation and loss distribution in and downstream of the passage revealed that the profile contouring and endwall jets primarily reduced the lower loss core associated with the passage vortex structure. The optimized endwall contour on the other hand resulted in a larger loss reduction and acted to primarily reduce the upper loss core associated with the strong corner separation noted in the baseline planar endwall flow case.

Together the present paper shows that each loss reduction technique developed for the front-loaded high-lift research airfoil was effective at minimizing aerodynamic losses in the endwall region. Furthermore, the secondary loss mechanisms addressed by each technique differed, providing insight into the application of endwall loss mitigation strategies in highly loaded designs.

Nomenclature

f = frequency
p = pressure
u = in-plane lateral velocity component
v = in-plane vertical velocity component
w = out-of-plane velocity component
x = axial coordinate
y = pitchwise coordinate
z = spanwise coordinate
D = diameter
N = number of jets
Q = Q-criterion
S = pitch/spacing
U = velocity magnitude
C_x = axial chord
C_μ = momentum coefficient
F^+ = reduced frequency
BR = blowing ratio
DC = measured duty cycle
SSL = suction side length
TKE = turbulent kinetic energy
γ = pressure loss coefficient
Δ = difference
ρ = density

Subscripts

in = inlet freestream
j = jet
out = exit freestream
PS = passage/pressure surface
$2D$ = pitchwise integrated

Superscripts

$\sim$ = phase-locked ensemble averaged
$^-$ = time-averaged
$'$ = secondary coordinate system

References

[1] Curtis, E. M., Hodson, H. P., Banieghbal, M. R., Denton, J. D., Howell, R. J., and Harvey, N. W., 1997, "Development of Blade Profiles for Low Pressure Turbine Applications," ASME J. Turbomach., **119**(3), pp. 531–538.

[2] Praisner, T. J., Grover, E. A., Knezevici, D. C., Popovic, I., Sjolander, S. A., Clark, J. P., and Sondergaard, R., 2013, "Toward the Expansion of the Low-Pressure-Turbine Airfoil Design Space," ASME J. Turbomach., **135**(6), p. 061007.

[3] Schmitz, J. T., Perez, E., Morris, S. C., Corke, T. C., Clark, J. P., Koch, P. J., and Puterbaugh, S. L. 2016, "Highly Loaded Low-Pressure Turbine: Design, Numerical, and Experimental Analysis," AIAA J. Propuls. Power, **32**(1), pp. 142–152.

[4] Langston, L. S., 2001, "Secondary Flow in Axial Turbines—A Review," Ann. N. Y. Acad. Sci., **934**(1), pp. 11–26.

[5] Rose, M. G., 1994, "Non-Axisymmetric Endwall Profiling in the HP NGVs of an Axial Flow Gas Turbine," Proceedings of the ASME 1994 IGTI and Aeroengine Congress and Exposition, Volume 1: Turbomachinery, The Hague, Netherlands, June 13–16, p. V001T01A090, ASME Paper No. 94-GT-249.

[6] Harvey, N. W., Rose, M. G., Taylor, M. D., Shahpar, S., Hartland, J. C., and Gregory-Smith, D. G., 1999, "Nonaxisymmetric Turbine End Wall Design: Part I—Three-Dimensional Linear Design System," ASME J. Turbomach., **122**(2), pp. 278–285.

[7] Praisner, T. J., Allen-Bradley, E., Grover, E. A., Knezevici, D. C., and Sjolander, S. A., 2013, "Application of Nonaxisymmetric Endwall Contouring to Conventional and High-Lift Turbine Airfoils," ASME J. Turbomach., **135**(6), p. 061006.

[8] Sauer, H., Muller, R., and Vogeler, K., 2000, "Reduction of Secondary Flow Losses in Turbine Cascades by Leading Edge Modifications at the Endwall," ASME J. Turbomach., **123**(2), pp. 207–213.

[9] Zess, G. A., and Thole, K. A., 2002, "Computational Design and Experimental Evaluation of Using a Leading Edge Fillet on a Gas Turbine Vane," ASME J. Turbomach., **124**(2), pp. 167–175.

[10] Lyall, M. E., King, P. I., Clark, J. P., and Sondergaard, R., 2014, "Endwall Loss Reduction of High Lift Low Pressure Turbine Airfoils Using Profile Contouring—Part I: Airfoil Design," ASME J. Turbomach., **136**(8), p. 081005.

[11] Sangston, K., Little, J., Lyall, M. E., and Sondergaard, R., 2014, "End Wall Loss Reduction of High Lift Low Pressure Turbine Airfoils Using Profile Contouring—Part II: Validation," ASME J. Turbomach., **136**(8), p. 081006.

[12] Marks, C. R., Sondergaard, R., Bear, P. S., and Wolff, M., 2016, "Reynolds Number Effects on the Secondary Flow of Profile Contoured Low Pressure Turbines," 54th AIAA Aerospace Sciences Meeting, San Diego, CA, AIAA Paper No. 2016-0114.

[13] Kawai, T., Shinoki, S., and Adachi, T., 1989, "Secondary Flow Control and Loss Reduction in a Turbine Cascade Using Endwall Fences," JSME Int. J., Ser. II, **32**(3), pp. 375–387.

[14] Chung, J. T., Simon, T. W., and Buddhavarapu, J. J., 1991, "Three-Dimensional Flow Near the Blade/Endwall Junction of a Gas Turbine: Application of a Boundary Layer Fence," Proceedings of the ASME 1991 IGTI and Aeroengine Congress and Exposition, Volume 4: Heat Transfer; Electric Power, Industrial Cogeneration, Orlando, FL, June 3–6, p. V004T09A008, ASME Paper No. 91-GT-045.

[15] Bloxham, M. J., and Bons, J. P., 2010, "Combined Blowing and Suction to Control Both Midspan and Endwall Losses in a Turbomachinery Passage," Proceedings of the ASME Turbo Expo 2010: Power for Land, Sea, and Air, Volume 7: Turbomachinery, Parts A, B, and C, Glasgow, UK, June 14–18, pp. 1609–1618, ASME Paper No. GT2010-23552.

[16] Benton, S. I., Bons, J. P., and Sondergaard, R., 2013, "Secondary Flow Loss Reduction Through Blowing for a High-Lift Front-Loaded Low Pressure Turbine Cascade," ASME J. Turbomach., **135**(2), p. 021020.

[17] Benton, S. I., Bernardini, C., Bons, J. P., and Sondergaard, R., 2014, "Parametric Optimization of Unsteady End Wall Blowing on a Highly Loaded Low-Pressure Turbine," ASME J. Turbomach., **136**(7), p. 071013.

[18] Gross, A., Marks, C., and Sondergaard, R., 2017, "Numerical Simulations of Active Flow Control for Highly Loaded Low-Pressure Turbine Cascade," 55th AIAA Aerospace Sciences Meeting, Grapevine, TX, AIAA Paper No. 2017-1460.

[19] Fletcher, N. N., Marks, C., Petrie, R., Sondergaard, R., and Wolff, M., 2018, "Experimental Investigation of Endwall Flow Control for Front Loaded Turbine Blades," 2018 AIAA Joint Propulsion Conference, Cincinnati, OH, AIAA Paper No. 2018-4436.

[20] Donovan, M. H., Wolff, M., Marks, C. R., Sondergaard, R., and Veley, E., 2019, "Periodic Forcing of an Endwall Vortex in a Highly Loaded Low Pressure Turbine," AIAA Scitech 2019 Forum, San Diego, CA, AIAA Paper No. 2019-0621.

[21] Babcock, H. J., Reeder, M., Thomas, L. M., and Marks, C. R., 2019, "Investigation of Loss Reduction in a High Lift Turbine by Localized Endwall Jets," AIAA Propulsion and Energy 2019 Forum, Indianapolis, IN, AIAA Paper No. 2019-4005.

[22] Bear, P., Wolff, M., Gross, A., Marks, C. R., and Sondergaard, R., 2018, "Experimental Investigation of Total Pressure Loss Development in a Highly Loaded Low-Pressure Turbine Cascade," ASME J. Turbomach., **140**(3), p. 031003.

[23] Dickel, J. A., Marks, C., Clark, J., Sondergaard, R., and Wolff, M., 2018, "Non-Axisymmetric Endwall Contouring of Front-Loaded High-Lift Low Pressure Turbines," 2018 AIAA Aerospace Sciences Meeting, Kissimmee, FL, AIAA Paper No. 2018-2125.

[24] Dickel, J. A., Marks, C., Sondergaard, R., and Wolff, M., 2018, "Optimization of a Non-Axisymmetric Endwall Contour for Front-Loaded High-Lift Low Pressure Turbines," 2018 AIAA Joint Propulsion Conference, Cincinnati, OH, AIAA Paper No. 2018-4918.

[25] Fletcher, N., Marks, C. R., and Donovan, M. H., 2020, "Secondary Flow Response to Endwall Jets in a Low Pressure Turbine," Proceedings of the ASME Turbo Expo 2020: Turbomachinery Technical Conference and Exposition, Volume 2B: Turbomachinery, Virtual, Online, Sept. 21–25, p. V02BT33A018, ASME Paper No. GT2020-15284.

[26] McQuilling, M. W., 2007, "Design and Validation of a High-Lift Low-Pressure Turbine Blade," Ph.D. dissertation, Wright State University, Dayton, OH.

[27] Gross, A., Marks, C. R., Sondergaard, R., Bear, P. S., and Wolff, J. M., 2018, "Experimental and Numerical Characterization of Flow Through Highly Loaded Low-Pressure Turbine Cascade," AIAA J. Propuls. Power, **34**(1), pp. 27–39.

[28] Gross, A., Marks, C. R., and Sondergaard, R., 2017, "Numerical Investigation of Low-Pressure Turbine Junction Flow," AIAA J., **55**(10), pp. 3617–3621.

[29] Veley, E., Marks, C., Anthony, R., Sondergaard, R., Fletcher, N., and Wolff, M., 2018, "Unsteady Flow Measurements in a Low Pressure Turbine Passage," AIAA Paper No. 2018-2124.

[30] Bear, P. S., Wolff, M., Gross, A., Marks, C., and Sondergaard, R., "The Effect of Profile Contouring on Secondary Flow Structures in Low Pressure Turbines," 54th AIAA Aerospace Sciences Meeting, San Diego, CA, AIAA Paper No. 2016-0113.

[31] Hirsch, C., ed., 1993, "Advanced Methods for Cascade Testing," AGARD Rept. AGARD-AG-328.

[32] Lyall, M. E., 2012, "Effects of Front-Loading and Stagger Angle on Endwall Losses of High Lift Low Pressure Turbine Vanes," Ph.D. dissertation, Air Force Institute of Technology, Wright-Patterson AFB, OH.

[33] Hunt, J. C., Wray, A. A., and Moin, P., 1988, "Eddies, Streams, and Convergence Zones in Turbulent Flows," Studying Turbulence Using Numerical Simulation Databases—II Proceedings of the 1988 Summer Program, pp. 193–208.

[34] Sieverding, C. H., 1985, "Recent Progress in the Understanding of Basic Aspects of Secondary Flows in Turbine Blade Passages," ASME J. Eng. Gas Turbines Power, **107**(2), pp. 248–257.